



# Velocity measurement of near-wall flow over inclined and curved boundaries by extended interfacial particle image velocimetry

Thien Duy Nguyen<sup>a,\*</sup>, John Craig Wells<sup>a</sup>, Chuong Vinh Nguyen<sup>b</sup>

<sup>a</sup> Department of Civil and Environmental Engineering, Ritsumeikan University, 1-1-1 Noji Higashi, Kusatsu, Shiga, Japan

<sup>b</sup> Department of Mechanical and Aeronautical Engineering, Monash University, VIC 3800, Australia

## ARTICLE INFO

### Article history:

Received 10 October 2011

Received in revised form

12 December 2011

Accepted 28 December 2011

### Keywords:

Near-wall

Curved boundary

Interfacial PIV

## ABSTRACT

Particle image velocimetry (PIV) measurements near a curved boundary usually require efforts to deal with low tracer density, high shear gradient and wall reflection. To resolve these difficulties, we presented a near-wall measurement technique named interfacial PIV (IPIV) that could return a tangential velocity component and a tangential component of wall gradient [Nguyen TD, Wells J, Nguyen C. Wall shear stress measurement of near-wall flow over inclined and curved boundaries by stereo interfacial particle image velocimetry. *International Journal of Heat and Fluid Flow* 2010;31(3):442–9]. In this paper, we introduce an extension of IPIV to measure the tangential and wall-normal velocity components. This extension allows IPIV to obtain three velocity components when IPIV is applied to stereoscopic PIV images of flows over inclined and curved boundaries. The performance of IPIV is validated against a particle image distortion (PID) technique using synthetic images generated from a direct numerical simulation velocity field of a turbulent flow over a wavy wall. Results show that IPIV is more accurate than PID in the near-wall velocity measurement. Practical applications of IPIV to experimental images of open flume tests with a wavy wall and a backward-facing step are described.

© 2012 Elsevier Ltd. All rights reserved.

## 1. Introduction

Near-wall measurements are of great interest in many engineering applications. However, particle image velocimetry (PIV) measurement at near-wall regions is often difficult. Difficulties such as insufficient image particles, high velocity gradient and wall reflection are enhanced when PIV is performed near a curved wall.

With an aim to increase the spatial resolution of PIV to the low particle density and laminar flows, Westerweel et al. [1] first implemented a two-point ensemble correlation technique to obtain a single-pixel resolution, i.e. one velocity vector per pixel. Tested on the synthetic and real images of a steady flow, the single-pixel correlation required a large number of image samples to yield a reliable correlation peak [2]. Billy et al. [3] applied the single pixel resolution correlation to a non-laminar flow—a steady on average Poiseuille flow in a small grooved channel. However, the authors showed that this technique was not well adapted and its accuracy was in the range of  $\pm 1$  pixel compared to the standard cross-correlation algorithm.

To improve the accuracy of the cross-correlation algorithm when applied to the high velocity gradient flows, Huang et al. [4] introduced particle image distortion (PID). The PID technique uses information on flow patterns initially obtained by the standard cross-correlation, then deforms image template to compensate iteratively particle displacements. However, compared to the standard cross-correlation technique, PID often requires more computation time during its iteration.

The standard cross-correlation technique often yields erroneous velocity vectors if it is applied to the near-wall region and the interrogation windows contain the wall boundary intensity [5]. To reduce the effect of the wall interface to the correlation calculation, Gui et al. [6] used a binary mask to distinguish the fluid and the solid wall regions in the image template. The masking technique led to an increase in the cross-correlation quality. However, it is favourable to eliminate the appearance of the wall interface in the correlation process. To completely exclude the wall intensity from the correlation calculation, Theunissen et al. [7] employed an unstructured grid and adapted the size of the image template as a function of the velocity gradient, and then oriented the interrogation window parallel to the boundary.

To deal with the near-wall flows and the curved boundaries, Nguyen et al. [8] introduced the interfacial PIV (IPIV) that included an image transformation and a novel one-dimensional (1D) cross-correlation (line correlation) technique. The image transformation is used to stretch a curved image segment into a rectangle. From

\* Correspondence to: University of Lille North of France, Faculty of ENSIAME, TEMPO laboratory, Le Mont Houy, 59313Valenciennes, CEDEX 9, France. Tel.: +33 6 20 95 12 08.

E-mail address: [thien.duy.ng@gmail.com](mailto:thien.duy.ng@gmail.com) (T.D. Nguyen).

the transformed images, the 1D correlation is applied to produce a correlation stack that reveals particles' displacements in the tangential direction. The tangential component of wall gradient is derived by fitting a straight line on the correlation stack and searching for the slope of the straight line that maximizes the sum of the correlation peaks along with it. The near-wall tangential velocity profile is determined by integrating the velocity gradients, which are iteratively measured by the line-fitting algorithm. An experimental application of IPIV to measure the wall shear in a model carotid artery was shown by Buchmann et al. [9]. Recently, Nguyen et al. [10] extended the IPIV technique to measure two components of the wall gradient by a stereo reconstruction. The obtained wall gradients were used to build the measurement model that related the velocity fields and the wall gradients in a backward-facing step flow [11].

In this paper, we introduce an extension of IPIV to measure the tangential and wall-normal velocity components based on the line correlation. This extension allows IPIV to obtain three velocity components with a single pixel resolution in the wall-normal direction when IPIV is applied to stereoscopic PIV images of flows over an inclined and a curved boundary. We validate the extended IPIV against the PID technique by using stereoscopic synthetic images generated from a DNS velocity snapshot of a turbulent flow over a wavy wall. Practical applications of the extended IPIV technique to experimental images taken from open flume tests with a wavy wall and a backward-facing step are presented.

## 2. Extended interfacial particle image velocimetry

In this section, we describe the extended IPIV technique to measure the velocity profile near a curved boundary. Given a set of PIV image pairs captured by stereoscopic cameras, one can apply the basis steps of the extended PIV as following.

1. Dewarping the PIV images captured by the stereo cameras.
2. Identifying the wall boundary.
3. Conformally transforming the near-wall image region into a rectangle shape to handle the inclined or the curved boundary.
4. Line-correlating the first and second exposures, and then measuring the tangential and wall-normal displacements from the correlation stacks.
5. Reverse transforming the displacements obtained in the transformed domain to the projected domain.
6. Stereo-reconstructing to obtain the physical velocity profiles.

In this procedure, steps 2–5 can be applied directly to PIV images captured by one camera. In step 1, we apply an image mapping algorithm described in [12] to map the recorded PIV image onto the object plane. The dewarped image of each angular camera is no longer distorted and has a constant magnification. In step 2, we employ the second-order wall detection algorithm called Laplacian of Gaussian to identify the positions of the boundary. Details of an algorithm to identify an arbitrarily moving wall can be reviewed in [13].

### 2.1. Transforming near-wall image to rectangle

Given a near-wall flow region with an identified boundary curvature shown in Fig. 1(a), we use a Matlab open source SeaGrid developed by Denham [14] to generate an orthogonal curvilinear grid based on the enclosed boundaries and the number of segments on each contour. The curved image segment, namely the projected physical domain  $(x, y)$ , is then conformally transformed into the rectangular image, namely the transformed domain  $(\xi, \eta)$ . Intensities of the transformed image (Fig. 1(b)) are produced by a bi-cubic interpolation from the corresponding intensities of the curved image inside the grid region. The Jacobian of the transformation is calculated as

$$J = \det \begin{vmatrix} \partial x / \partial \xi & \partial x / \partial \eta \\ \partial y / \partial \xi & \partial y / \partial \eta \end{vmatrix} = \frac{\partial x}{\partial \xi} \frac{\partial y}{\partial \eta} - \frac{\partial x}{\partial \eta} \frac{\partial y}{\partial \xi}. \quad (1)$$

The transformed image has a rectangular shape, which can be applied by any PIV technique.

### 2.2. Measuring displacements from line-correlation stacks

In this step, we first then perform a 1D cross-correlation, i.e. line correlation, between horizontal pixel lines of the first exposure template and those of the second exposure template to produce a wall-parallel "stack" of 1D correlation curves. The covariance  $C_{U,n}$  ( $n = 1, N$ ) is calculated by

$$C_{U,n} = \sum_{m=1}^M (I_{m+U,n} - \bar{I}_{U,n})(I'_{m,n} - \bar{I}'_n), \quad (2)$$

where  $(M, N)$  are the width and height of the template,  $(m, n)$  are the horizontal and vertical pixel coordinates of the template,  $\bar{I}_{U,n}$  and  $\bar{I}'_n$  are the mean intensities on each horizontal pixel line of the first and second templates, respectively. In order to reduce the peak-locking effect in the velocity measurement, we apply the continuous window shift algorithm [15], i.e. subpixel intensity of the second exposure template is interpolated and used in the cross-correlation. In this paper, we normalize the covariance  $C_{U,n}$  with the root mean square (r.m.s) of  $(I_{m+U,n} - \bar{I}_{U,n})$  and the r.m.s of  $(I'_{m,n} - \bar{I}'_n)$  to increase the signal-to-noise ratio. A colourmap of the wall-parallel correlation stack is shown in Fig. 1(c).

With an assumption on the wall-normal inter-frame tracer displacement being less than particle image diameter, a purely tangential search of the line correlation can produce a peak. This condition can be obtained by reducing the time interval between the first and second exposures. Peaks on the wall-parallel correlation stack correspond to the tracers' displacements in the tangential direction. A peak detection is performed to search for the local maximal peak values on the wall-parallel correlation stack. In order to derive the tangential displacement  $U$ , we implement the detected peak values into a Gaussian kernel  $\Omega$  with a width  $\sigma$  expressed in Eq. (3). The calculation of the tangential displacement  $U$  at a vertical position  $n$  is shown by Eq. (4),

$$\Omega(y - n) = \exp \left[ -\frac{(y - n)^2}{2\sigma^2} \right], \quad (3)$$

$$U(n) = \frac{\sum_{y_i=1}^{y_i=N} U(y_i) \Omega(y_i - n) P_U(y_i)}{\sum_{y_i=1}^{y_i=N} \Omega(y_i - n) P_U(y_i)}, \quad (4)$$

where  $P_U(y_i)$  is a peak value at the vertical position  $y_i$  in the wall-parallel correlation stack. Fig. 1(c) shows the detected peaks (black asterisks) and the tangential displacement profile  $U$  (white curve) overlotted on the wall-parallel correlation stack.

Next, we shear the second exposure image template parallel to the wall based on the obtained tangential displacement  $U$ . It is necessary to note that the image intensity of the sheared template is interpolated from the originally transformed image to reduce the image quality loss. We then cross-correlate a horizontal pixel line at a given height  $n$  in the first exposure template with other horizontal pixel lines at a vertical height  $n + V$  in the second exposure template to yield a wall-normal stack of 1D correlation curves. The covariance  $C_{V,n}$  ( $n = 1, N$ ) is calculated by

$$C_{V,n} = \sum_{m=1}^M (I_{m,n} - \bar{I}_{V,n})(I'_{m,n+V} - \bar{I}'_{n+V}), \quad (5)$$

where  $(M, N)$  are the width and height of the template,  $(m, n)$  are the horizontal and vertical pixel coordinates of the template,

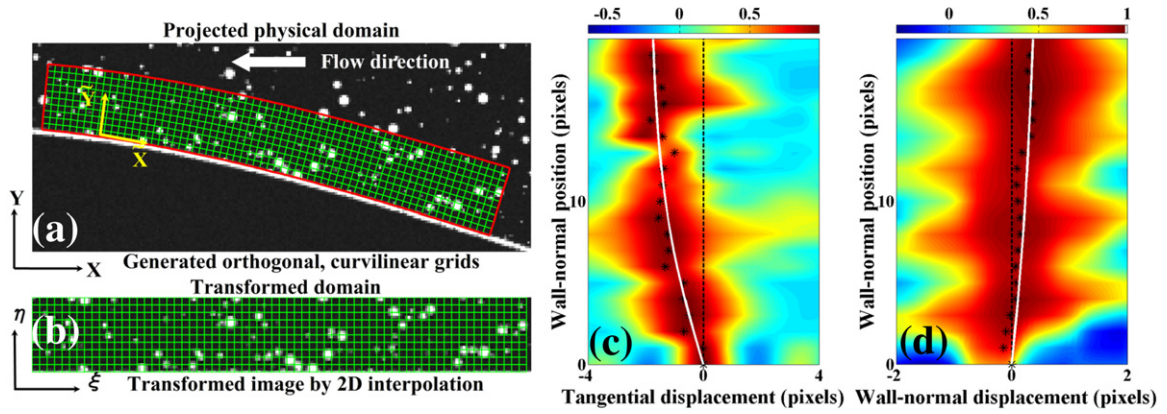


**Fig. 1.** Image transformation and near-wall velocity measurements by the extended IPIV, (a) generated orthogonal curvilinear grid, (b) transformed image by 2D interpolation, measurements of tangential (c) and wall-normal (d) displacements from corresponding correlation stacks.

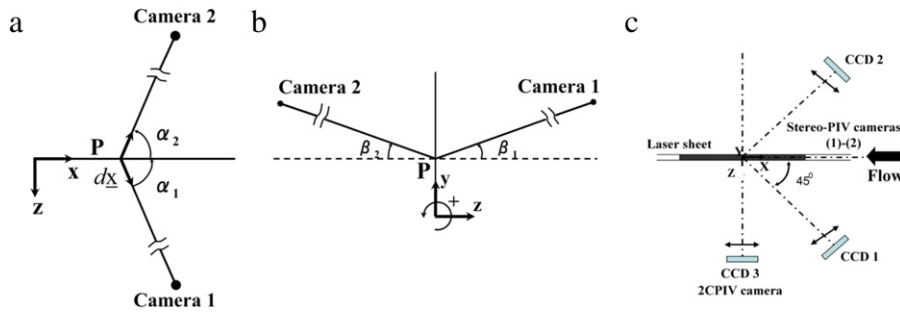


**Fig. 2.** (a), (b) Geometric positions of cameras and local viewing angles, (c) camera projections for generating synthetic images.

$\bar{I}_{U,n}$  and  $\bar{I}_n$  are the mean intensities on each horizontal pixel line of the first and second templates, respectively. Fig. 1(d) shows a colourmap of the wall-normal correlation stack. Peaks on the wall-normal correlation stack contain the information of particles' displacements in the wall-normal direction. A peak detection is then performed on the wall-normal correlation stack. The wall-normal displacement  $V$  at a vertical position  $n$  is calculated by using the detected peak values and the Gaussian kernel  $\Omega$  as below

$$V(n) = \frac{\sum_{y_i=1}^{y_i=N} V(y_i)\Omega(y_i - n)P_V(y_i)}{\sum_{y_i=1}^{y_i=N} \Omega(y_i - n)P_V(y_i)} \quad (6)$$

where  $P_V(y_i)$  is a peak value at the vertical position  $y_i$  in the wall-normal correlation stack. In Fig. 1(d), the detected peaks are illustrated by the black asterisks and the measured wall-normal displacement  $V$  is shown by the white curve.

### 2.3. Reverse transforming the displacements to projected domain

Once the tangential and wall-normal displacements,  $U$  and  $V$  respectively, are determined, a reverse transformation is necessitated to obtain the projected values,  $u$  and  $v$ , of the physical velocity. The projected displacements,  $u$  and  $v$ , are calculated by

$$u = \frac{1}{J} \left( \frac{\partial x}{\partial \xi} U + \frac{\partial x}{\partial \eta} V \right) \quad (7)$$

$$v = \frac{1}{J} \left( \frac{\partial y}{\partial \xi} U + \frac{\partial y}{\partial \eta} V \right) \quad (8)$$

where  $U$  and  $V$  are the tangential and the wall-normal displacements measured in the transformed domain.

### 2.4. Stereo-reconstructing to obtain physical velocity profiles

For the stereoscopic PIV application, after the reverse transformation, one obtains two components of the projected velocities, called  $(u_1, v_1)$  for camera 1 and  $(u_2, v_2)$  for camera 2. In order to obtain three components  $(u, v, w)$  of the physical velocity, we apply a stereo reconstruction by means of geometrical considerations proposed by Willert [16]. This reconstruction is expressed by

$$u = \frac{u_1 \tan \alpha_2 - u_2 \tan \alpha_1}{\tan \alpha_2 - \tan \alpha_1}, \quad (9)$$

$$w = \frac{u_1 - u_2}{\tan \alpha_2 - \tan \alpha_1}, \quad (10)$$

$$v = \frac{v_1 \tan \beta_2 - v_2 \tan \beta_1}{\tan \beta_2 - \tan \beta_1}, \quad (11)$$

where  $\alpha_1, \alpha_2$  are the angles between the viewing rays from camera 1, camera 2 and the  $XY$  plane measured in the  $XZ$  plane, and  $\beta_1, \beta_2$  are the angles between the viewing rays from camera 1, camera 2 and the  $XZ$  plane measured in the  $YZ$  plane, respectively. Fig. 2(a), (b) illustrate these viewing angles from the stereoscopic cameras to a generic point  $P$  located on the measurement plane. In order to evaluate the local viewing angles  $\alpha_{1,2}$  and  $\beta_{1,2}$  in Eqs. (9)–(11), we apply a technique proposed by Giordano and Astarita [17]. For the point  $P$  on the measurement plane viewed by camera 1, the local viewing angles  $\alpha_1$  and  $\beta_1$  of camera 1 can be determined as

$$\tan \alpha_1 = \left( \frac{\partial z}{\partial x} \right)_{dX_1=0} = \frac{\frac{\partial Y}{\partial y} \frac{\partial X}{\partial x} - \frac{\partial Y}{\partial x} \frac{\partial X}{\partial y}}{\frac{\partial Y}{\partial z} \frac{\partial X}{\partial y} - \frac{\partial Y}{\partial y} \frac{\partial X}{\partial z}}, \quad (12)$$

$$\tan \beta_1 = \left( \frac{\partial z}{\partial y} \right)_{dX_1=0} = \frac{\frac{\partial Y}{\partial x} \frac{\partial X}{\partial y} - \frac{\partial Y}{\partial y} \frac{\partial X}{\partial x}}{\frac{\partial Y}{\partial z} \frac{\partial X}{\partial y} - \frac{\partial Y}{\partial y} \frac{\partial X}{\partial z}}. \quad (13)$$

A similar calculation can be performed for the angles  $\alpha_2$  and  $\beta_2$  of camera 2. Three components ( $u$ ,  $v$ ,  $w$ ) of the physical velocity can be determined by substituting the obtained local viewing angles  $\alpha_1$ ,  $\alpha_2$  and  $\beta_1$ ,  $\beta_2$  into Eqs. (9)–(11).

### 3. Test with synthetic images

In order to test the extended IPIV technique, synthetic images of  $400 \times 400$  pixels were generated from a DNS snapshot of a turbulent flow over a wavy bed [18,19]. The wavy boundary consisted of three wavelengths and the ratio of the peak-to-peak amplitude to the wavelength was 0.1 yielding a maximum slope of 0.31. The Reynolds number  $Re_H$  based on the bulk velocity  $U_m$  and the flow depth  $H$  was 6760 while that based on the friction velocity and the peak-to-peak height was 106. Images and particle displacements were synthetically projected from a field of view of  $0.4H \times 0.4H$  ( $H = 50$  mm) at the left-side of the central wavelength, where the highest shear flow region was. In the synthetic image generator, particle image patterns and camera projection models proposed by Lecordier and Westerweel [20] were implemented. The first set included forty 2C PIV image pairs (perpendicular projection) and the second set included forty stereoscopic PIV image pairs (oblique projection) with the effect of the perspective and distortion caused by the angular stereoscopic configuration. Fig. 2(c) illustrates the camera projection for generating synthetic images. Laser sheet had a Gaussian intensity profile with  $\sigma = 0.5$  mm. Particles, of which diameter had a Gaussian distribution of  $\sigma = 1.28$  pixels, a mean value of 3.2 pixels and varied from 2.2 to 6 pixels, were randomly scattered into a virtual 3D volume of the laser sheet. Seeding density was about 0.01 particle/pixel. Background noise with a Gaussian distribution of  $\sigma = 2.5$  was also added to the images. The intensity levels of the background noise were based on our experimental images with the minimum and maximum values of 30 and 45 greyscale units, respectively. A time delay of  $\Delta t = 1$  ms was chosen to yield the maximal tracer displacements of about 5 pixels.

In the applications of the extended IPIV to the synthetic images, for the set of 2C PIV images, the processes from steps 2 to 5 were performed directly. For the set of stereoscopic PIV images, the processes from steps 1 to 6 were applied. For both sets of synthetic images, the extended IPIV was performed on the near-wall image region. The interrogation window in the extended IPIV technique was  $50 \times 1$  pixels yielding about 66% overlap in the horizontal direction. The width of the Gaussian-weighted scheme in Eq. (3) was  $\sigma = 7$  pixels.

To evaluate the proposed technique, we compare the performances of the extended IPIV and particle image distortion [4]. For the set of 2C PIV images, PID was performed on the transformed rectangular images which were advantageously resulted by the step 3 of the extended IPIV technique. Two velocity components  $U$  and  $V$  obtained by the PID technique were reverse-transformed to the projected domain by step 5. For the set of stereoscopic PIV images, after dewarping the images, we performed PID on the rectangular images, which were favourably transformed by the step 3. In this case, the reverse transformation was followed by the stereo reconstruction in order to obtain the physical velocity profiles. For both applications of PID, we used a regular grid, of which the grid spacing in the horizontal direction was equal to that used in the extended IPIV and the grid spacing in the vertical direction was 5-pixel interval. The interrogation window of PID was chosen as  $50 \times 11$  pixels yielding about 66% and 50% overlaps in the horizontal and the vertical directions, respectively. At the grid locations nearest to the wall, the window size was adapted to  $50 \times 8$  pixels to resolve small particles' displacements in this region and still contain enough particles.

**Table 1**

Random and total errors of velocity measurements by the extended IPIV and PID techniques.

	$\epsilon_{rand}$ (pixel/ $\Delta t$ )			$\epsilon_{total}$ (pixel/ $\Delta t$ )		
	$u_{rand}$	$v_{rand}$	$w_{rand}$	$u_{total}$	$v_{total}$	$w_{total}$
PID to set 1	0.127	0.073		0.237	0.085	
PID to set 2	0.066	0.041	0.075	0.125	0.062	0.112
IPIV to set 1	0.065	0.048		0.139	0.054	
IPIV to set 2	0.056	0.026	0.048	0.107	0.033	0.057

In this paragraph, we evaluate the performances of PID and the extended IPIV in terms of a random error,  $\epsilon_{rand}$ , and a total error,  $\epsilon_{total}$ . The random error,  $\epsilon_{rand}$ , is defined as the r.m.s of the total averaged difference between  $\mathbf{u}(n)_p^q$  and the ensemble-averaged,  $\overline{\mathbf{u}(n)^q}$ . It can be expressed as:

$$\epsilon_{rand} = \sqrt{\frac{1}{N_v P Q} \sum_{n=1}^{N_v} \sum_{q=1}^Q \sum_{p=1}^P (\mathbf{u}(n)_p^q - \overline{\mathbf{u}(n)^q})^2}, \quad (14)$$

where  $\mathbf{u}$  is the velocity vector,  $N_v$ ,  $Q$  are the numbers of measurement points in the vertical and streamwise directions respectively, and  $P$  is the number of image pairs. The ensemble-averaged velocity  $\overline{\mathbf{u}(n)^q}$  is calculated by

$$\overline{\mathbf{u}(n)^q} = \frac{1}{P} \sum_{p=1}^P \mathbf{u}(n)_p^q. \quad (15)$$

The total error  $\epsilon_{total}$  is defined as the r.m.s of the total averaged difference between  $\mathbf{u}(n)_p^q$  and the DNS velocity  $\mathbf{u}_{DNS}^q$ , and expressed as:

$$\epsilon_{total} = \sqrt{\frac{1}{N_v P Q} \sum_{n=1}^{N_v} \sum_{q=1}^Q \sum_{p=1}^P (\mathbf{u}(n)_p^q - \mathbf{u}_{DNS}^q)^2}. \quad (16)$$

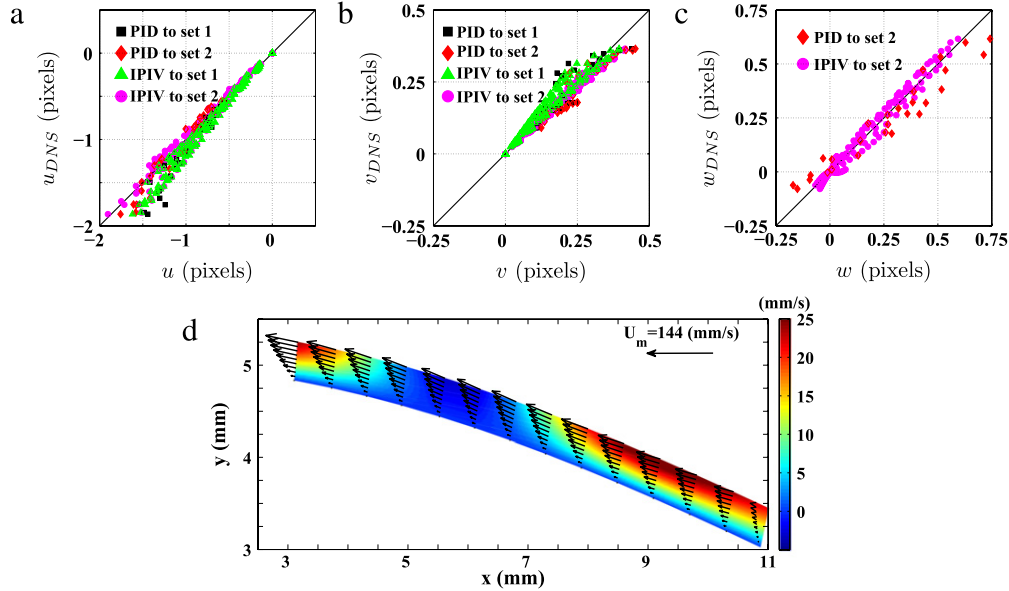
As the extended IPIV technique is designed for the near-wall flow measurement, we choose to compare velocities measured by the extended IPIV and PID within a near sub-layer region—about 10 wall units. This yields  $Q = 14$ ,  $P = 40$  and  $N_v = 10$  for the extended IPIV and  $N_v = 2$  for the PID technique.

Fig. 3(a)–(c) show the comparisons among the DNS velocity data and three velocity components ( $u$ ,  $v$ ,  $w$ ) by applying the PID and the extended IPIV techniques to the set 1 and set 2. In these figures, data points represent the ensemble-averaged velocity. The computed random error and total error are shown in Table 1. For the measurements on set 1, the extended IPIV had the total errors of  $(\epsilon_{total,u}, \epsilon_{total,v}) = (0.139, 0.054)$  pixels, which were 40% smaller than the total errors of PID and less than 3% of the maximal particle displacements. For the measurements on set 2, the total errors of the extended IPIV were  $(\epsilon_{total,u}, \epsilon_{total,v}, \epsilon_{total,w}) = (0.107, 0.033, 0.057)$ , which were about 20% to 40% smaller than those of PID.

From the comparisons between the PID and the extended IPIV velocity measurements, it is shown that the extended IPIV yielded more accurate results than PID in the very near-wall region.

### 4. PIV experiments

In this section, we describe two practical applications of the extended IPIV technique to two experimental PIV image sets. The first set was 2C PIV images taken from a wavy-bed experiment. The second set was stereoscopic PIV images taken from a backward-facing step experiment. In addition to performing the extended IPIV, we applied PID and recursive PIV techniques to the far-wall image regions of these image sets. Results of the extended IPIV were compared to those of the PID and the recursive PIV obtained at grid points nearest to wall boundaries.



**Fig. 3.** Comparisons among DNS data and velocity measurements by the PID and the extended IPIV techniques, (a) tangential velocity component  $u$ , (b) wall-normal velocity component  $v$ , (c) spanwise velocity component  $w$ , (d) near-wall velocity measured by the extended IPIV, vectors are the tangential and wall-normal velocity components, colour is the spanwise velocity component.

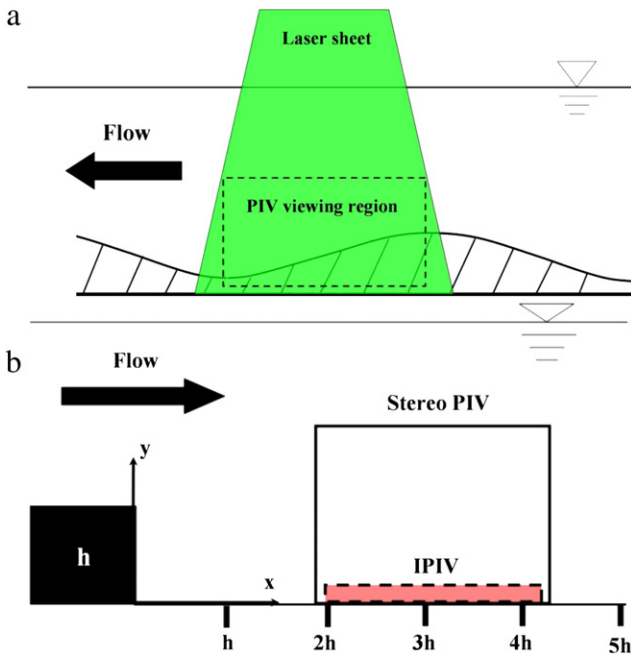


**Fig. 4.** PIV experiments. (a) Wavy-bed experiment, (b) backward-facing step experiment.

#### 4.1. Wavy-bed experiment

The first set included 320 images captured from a turbulent flow over an acrylic-plastic wavy bed in an open water channel. The wavelength was  $\lambda = 50$  mm with a peak-to-peak amplitude of  $\delta = 5$  mm. Experimental configuration is shown in Fig. 4(a). Reynolds number based on the wall shear stress and the incoming flow was about 300. Hollow glass sphere particles with a mean diameter of  $10 \mu\text{m}$  seeded the water flow. A double pulsed Nd:YAG laser illuminated a 2-mm-thick vertical sheet of the flow in the mid-plane of the test section. The fluid region in the central plane was imaged by a Kodak Megaplug Model ES1.0 charge couple device (CCD) camera with a resolution of  $1000 \times 1008$  pixels. Particle image diameter varied from 2 to 5 pixels. Seeding density was

about 0.004 particle/pixel. The maximum particle displacement was about 15 pixels. Only the near-wall image region of  $1008 \times 50$  pixels was processed (see Fig. 5(a)).

In this application, the interrogation window of the extended IPIV technique was  $100 \times 1$  pixels yielding 75% overlap in the horizontal direction. The width of the Gaussian scheme was  $\sigma = 7$  pixels. Fig. 5(a) shows an instantaneous velocity field obtained by the extended IPIV technique at the near-wall image region. The velocity vectors are shown for every 5 vertical grid lines for the visibility. The PID technique was performed on rectangular images, which were favourably transformed by the step 3 of the extended IPIV technique. The interrogation window of the PID technique was  $100 \times 11$  pixels, yielding 75% and 50% overlaps in the horizontal and vertical directions, respectively. At the first grid points nearest to the boundary, 5 pixels from wall, the PID template height was adapted to 8 pixels to account for small displacements. In the PID iterations, displacements were computed from the correlation map with a Gaussian peak fit [21] for sub-pixel accuracy. Vector validation was to apply a median filter [22] and a standard deviation filter to remove spurious vectors, and then fill in the blanks by interpolation.

Fig. 5(c), (d) show the comparisons of velocity components  $u$  and  $v$  obtained by the PID technique and those obtained by the extended IPIV. The maximal differences between the velocity measurements of the PID technique and those of the extended IPIV were  $(\Delta u, \Delta v) = (0.25, 0.10)$  pixel, respectively. The means of absolute velocity differences were  $(\langle |\Delta u| \rangle, \langle |\Delta v| \rangle) = (0.07, 0.04)$  pixel. An agreement between the extended IPIV and PID results obtained at the grid points in the buffer layer ( $5 < y^+ < 30$ ) shows that if the constraint in the wall-normal tracer displacement is satisfied, the extended IPIV is suitable for the velocity measurement not only in the sub-layer but also in the buffer layer.

Fig. 5(b) shows the mean velocity vectors computed from 320 velocity snapshots. Colour map illustrates the spanwise vorticity. Velocity vector  $U = -0.2 \text{ mm}/\Delta t$ , yielding an inter-frame displacement of 8 pixels, was also plotted for the scaling. A high shear gradient region was observed at the top of the wavy bed. In the valley of the wavy bed, a recirculation region appeared and a mean separation point was found at  $X_r = 16.7$  mm.

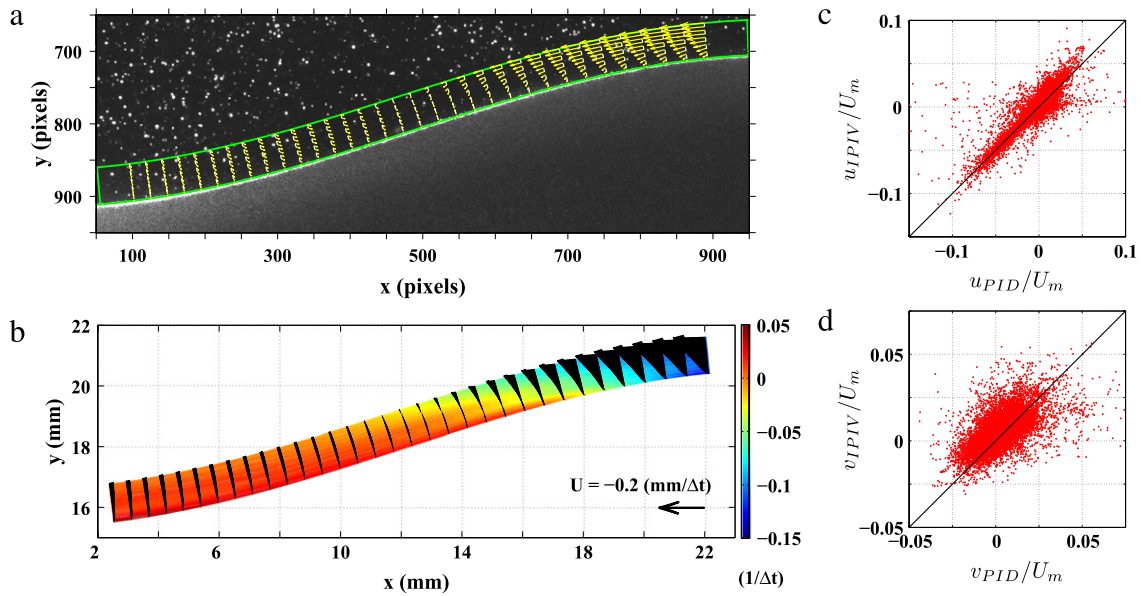


**Fig. 5.** Results from wavy-bed experiment. (a) Instantaneous velocity vectors measured by the extended IPIV, vectors are shown only 1 for every 5 vertical grid lines, (b) time-averaged velocity vectors, colour shows spanwise vorticity computed from time-averaged velocity vectors. Comparisons between the extended IPIV and the PID techniques (c)  $u$ , (d)  $v$ .

#### 4.2. Backward-facing step experiment

The second set included 1050 stereoscopic PIV image pairs taken from a turbulent flow over a backward-facing step in an open water channel. Experimental setup is sketched in Fig. 4(b). Reynolds number  $Re_h$  based on the mean streamwise velocity  $U_m$  and the step height  $h$  ( $h = 16.5$  mm) was about 2800. The coordinate origin was at the step corner with the streamwise, vertical and spanwise directions denoted by  $x$ ,  $y$  and  $z$ , respectively. Silver coated particles with a mean diameter of  $10 \mu\text{m}$  seeded the water flow. The fluid region in the central  $xy$  plane, with  $x/h$  ranging from 1.85 to 4.25, was illuminated by a double pulsed Nd:YAG laser and imaged by a stereoscopic PIV system. The stereoscopic PIV system was comprised of two Kodak Megaplug Model ES1.0 cameras with resolutions of  $1000 \times 1008$  pixels. In the stereo configuration, cameras viewed horizontally at  $45^\circ$  from downstream on either side of the channel, viewing through the water prisms on the sidewalls. The camera bodies were slightly rotated to satisfy the Scheimpflug condition. The sampling rate was set at 15 Hz and the time interval between the first and second exposures was  $\Delta t = 3$  ms yielding the maximum particle displacement of 8 pixels.

The stereoscopic PIV images were first dewarped by step 1 yielding the straight wall boundary in the resulted images. The near-wall image region of  $1000 \times 16$  pixels corresponding to a fluid flow within a region of  $y/h = 0.06$ , i.e. about 10 wall units, was processed by the extended IPIV technique. Particle image diameter varied from 2 to 4 pixels. Seeding density was about 0.005 particle/pixel.

The interrogation window of the extended IPIV technique was  $64 \times 1$  pixels, yielding 50% overlap in the horizontal direction. The width of the Gaussian kernel was 5 pixels. In this application, we applied a recursive PIV technique to the image set. The recursive PIV started with an interrogation window of  $64 \times 64$  pixels and ended with an interrogation window of  $32 \times 32$ . The first iteration initially computed the particle displacements, which were then used to shift the interrogation window in the second iteration. Both iterations had a 50% window overlap, resulting in a vector spacing of 1 mm. The first grid points of the recursive PIV closest to the wall were located at  $y/h = 0.06$ , about 10 wall units. In both of the iterations, vectors were computed from the correlation map with

a Gaussian peak fit [21] for sub-pixel accuracy. A median filter [22] and a standard deviation filter were applied to remove spurious vectors.

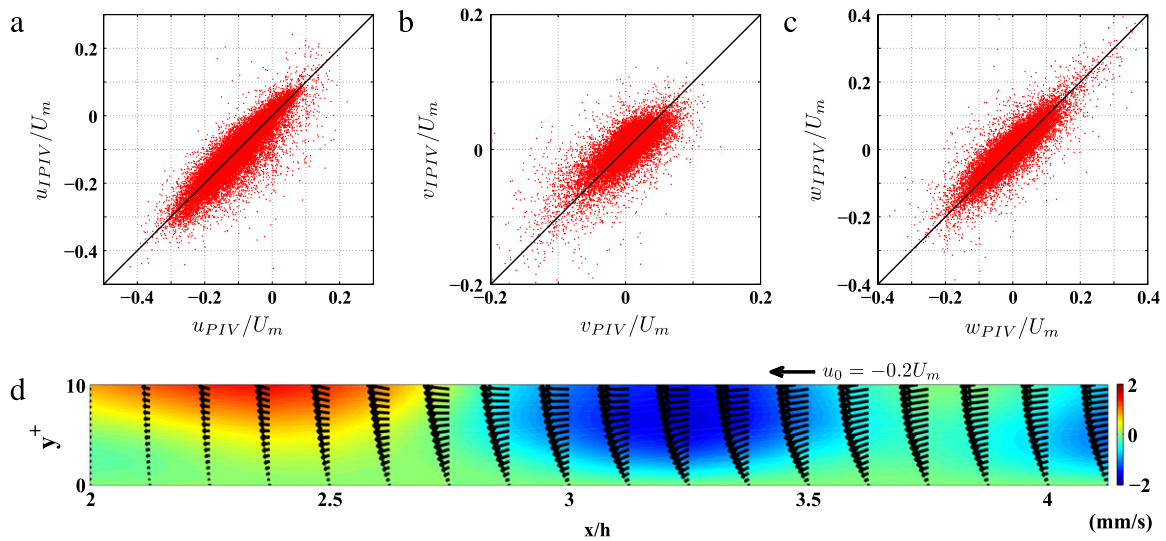
Fig. 6(a)–(c) show the comparisons of displacements  $u$ ,  $v$  and  $w$  obtained by the extended IPIV and displacements obtained by the recursive PIV technique at the grid points in the buffer layer. An agreement between these results indicates the capability of the extended IPIV technique that it can be applied in the buffer layer if the time interval is suitably chosen. The maximal differences between the velocity measurements of the extended IPIV and those of the recursive PIV were  $(\Delta u, \Delta v, \Delta w) = (0.19, 0.09, 0.08)$  pixels, respectively. The means of absolute velocity differences were  $(\langle |\Delta u| \rangle, \langle |\Delta v| \rangle, \langle |\Delta w| \rangle) = (0.13, 0.03, 0.03)$  pixels, respectively.

Fig. 6(d) shows the mean velocity field computed from 1050 image pairs. Vectors are the streamwise and wall-normal velocity components,  $u$  and  $v$  respectively. Colour shows the mean spanwise velocity component  $w$ . Velocity vector  $u_0 = -0.2U_m$ , yielding an inter-frame displacement of 1.6 pixels was overplotted for comparison. Fig. 6(d) illustrates a strong reversed flow region. In this region, the spanwise velocity component fluctuates within 2% of the mean velocity  $U_m$ . The reason is that the PIV measurement was performed at the middle plane of the channel width and the flow could be assumed as symmetry.

In this application, it was not necessary to perform the step 3 because the wall boundary, which was inclined in the stereoscopic images, became straight after the dewarped process of step 1. This case is chosen to demonstrate that the extended IPIV is not limited by a sufficient small angle between the wall plane and cameras' viewing rays as the previous version [10]. In addition, results from this geometry can serve as a reference for experimental configurations in which the wall boundary is inclined respectively to the viewing direction. One such configuration might be a diffuser or a smoothly varying backstep.

## 5. Conclusion

In this paper, we presented an extension of the IPIV technique to measure the near-wall tangential and wall-normal velocity components based on the line correlation. This improvement allows the extended IPIV technique to obtain three velocity



**Fig. 6.** Results from backward-facing step experiment. Comparisons between velocity components measured by the extended IPIV and those measured by the recursive PIV technique, (a)  $u$ , (b)  $v$ , (c)  $w$ . The mean velocity field measured by the extended IPIV is shown in (d), vectors are the mean streamwise and wall-normal velocity components, colour is the mean spanwise velocity component.

components with a single-pixel resolution in the wall-normal direction when IPIV is performed on stereoscopic PIV images. We validated the extended IPIV against the PID technique by using two sets of synthetic PIV images generated from a DNS velocity field. The first set was 2C PIV images and the second set was stereoscopic PIV images. The obtained results show that the extended IPIV is more accurate than PID in near-wall velocity measurement.

In the second part of this paper, we described the applications of the extended IPIV to two sets of real PIV images. The first image set was captured by one camera from an experiment with a wavy bed. The second image set was taken by stereoscopic cameras from an experiment with a backward-facing step. We compared the velocity measurements of the extended IPIV technique and those of the PID and the recursive PIV techniques. For two latter methods, velocity components were taken at the first grid points nearest to the wall boundaries. The results showed that the extended IPIV technique is suitable for the velocity measurement in the near-wall flow region.

In this paper, we have not discussed on the capability of the extended IPIV on wall gradient measurement. However, the proposed technique is able to return three components of wall gradient when it is applied to stereoscopic PIV images. By means of the mapping algorithm and the stereo reconstruction described in steps 1 and 6, respectively, the extended IPIV is not limited by a sufficient small angle between the wall plane and cameras' viewing rays as discussed in the previous version [10].

## References

- [1] Westerweel J, Poelma C, Lindken R. Two-point ensemble correlation method for  $\mu$ PIV applications. In: Proceedings of 11th int symp. on applications of laser techniques to fluid mechanics. 2002.
- [2] Westerweel J, Poelma C, Lindken R. Application of 2-point ensemble correlation PIV to micro-channel flow. In: Proceedings of 5th int symp. on particle image velocimetry. 2003.
- [3] Billy F, David L, Pineau G. Single pixel resolution correlation applied to unsteady flow measurements. Measurement Science and Technology 2004; 15(6):1039.
- [4] Huang H, Fiedler H, Wang J. Limitation and improvement of PIV. Experiments in Fluids 1993; 15(4):263–73.
- [5] Keane R, Adrian R. Theory of cross-correlation analysis of PIV images. Applied Scientific Research 1992; 49(3):191–215.
- [6] Gui L, Wereley S, Kim Y. Advances and applications of the digital mask technique in particle image velocimetry experiments. Measurement Science and Technology 2003; 14(10):1820.
- [7] Theunissen R, Scarano F, Riethmuller M. On improvement of PIV image interrogation near stationary interfaces. Experiments in Fluids 2008; 45(4): 557–72.
- [8] Nguyen C, Nguyen T, Wells J, Nakayama A. Interfacial PIV to resolve flows in the vicinity of curved surfaces. Experiments in Fluids 2010; 48(4):577–87.
- [9] Buchmann N, Jermy M, Nguyen C. Experimental investigation of carotid artery haemodynamics in an anatomically realistic model. International Journal of Experimental and Computational Biomechanics 2009; 1(2):172–92.
- [10] Nguyen TD, Wells J, Nguyen C. Wall shear stress measurement of near-wall flow over inclined and curved boundaries by stereo interfacial particle image velocimetry. International Journal of Heat and Fluid Flow 2010; 31(3):442–9.
- [11] Nguyen TD, Wells J, Mokhasi P, Rempfer D. Proper orthogonal decomposition-based estimations of the flow field from particle image velocimetry wall-gradient measurements in the backward-facing step flow. Measurement Science and Technology 2010; 21(11):115406.
- [12] Couderc S, Schon J. Back-projection algorithm with misalignment corrections for 2D3C stereoscopic PIV. Measurement Science and Technology 2001; 12(9): 1371–81.
- [13] Jeon Y, Sung H. PIV measurement of flow around an arbitrarily moving body. Experiments in Fluids 2010; 1–12.
- [14] Denham C. SeaGrid orthogonal grid maker for Matlab. Woods Hole Science Center, US Geological Survey; 2000.
- [15] Gui L, Wereley S. A correlation-based continuous window-shift technique to reduce the peak-locking effect in digital PIV image evaluation. Experiments in Fluids 2002; 32(4):506–17.
- [16] Willert C. Stereoscopic digital particle image velocimetry for application in wind tunnel flows. Measurement Science and Technology 1997; 8(12): 1465–79.
- [17] Giordano R, Astarita T. Spatial resolution of the stereo PIV technique. Experiments in Fluids 2009; 46(4):643–58.
- [18] Nakayama A, Sakio K. Simulation of flows over wavy rough boundaries. Annual research briefs, center for turbulence research. NASA Ames/Stanford University; 2002. p. 313–24.
- [19] Yokojima S. Modeling and simulation of turbulent open-channel flows emphasizing free-surface effects. Ph.D. Thesis. Japan: Kobe University; 2002.
- [20] Lecordier B, Westerweel J. The EUROPIV synthetic image generator (SIG). In: Stanislas M, Westerweel J, Kompenhans J, editors. Particle image velocimetry: recent improvements. 2003. p. 145–62.
- [21] Raffel M, Willert C, Wereley S, Kompenhans J. Particle image velocimetry: a practical guide. Springer Verlag; 2007.
- [22] Westerweel J. Efficient detection of spurious vectors in particle image velocimetry data. Experiments in Fluids 1994; 16(3):236–47.